nature astronomy
SUPPLEMENTARY INFORMATION
https://doi.org/10.1038/s41550-018-0414-3
In the format provided by the authors and unedited.

Galactic bulge preferred over dark matter for the Galactic centre gamma-ray excess

Oscar Macias[1]*, Chris Gordon[2], Roland M. Crocker[3], Brenna Coleman[2], Dylan Paterson[2], Shunsaku Horiuchi[1] and Martin Pohl[4,5]

[1]Center for Neutrino Physics, Department of Physics, Virginia Tech, Blacksburg, VA, USA. [2]School of Physical and Chemical Sciences, University of Canterbury, Christchurch, New Zealand. [3]Research School of Astronomy and Astrophysics, Australian National University, Canberra, Australia. [4]Institute of Physics and Astronomy, University of Potsdam, Potsdam-Golm, Germany. [5]DESY, Zeuthen, Germany. *e-mail: oscar.macias@vt.edu

Supplementary Information

1. Template Construction

We do not include the empirically-derived extended emission templates used by the Fermi-Collaboration when generating the publicly available version of the Galactic diffuse emission model provided for standard data analysis[8], because they were used to flatten residuals over larger regions of the sky than we are interested in this analysis and they are specifically constructed in support of the generation of the Fermi-LAT point-source catalogues.

HI and $\mathbf{H_2}$ Gas Column Density Templates: We investigate two different methods for constructing the gas map templates:

- Interpolation approach: this method has been used to produce the interstellar gas distribution models employed in most previous analyses of the GCE and is the standard approach employed in GALPROP and by the Fermi team.

  In the interpolation approach, the gas column density maps are produced using the method given in Appendix B of ref. 47. Atomic hydrogen column density is derived from the 21 cm LAB survey of Galactic HI[49]. Molecular hydrogen is traced by the 2.6 mm emission line of carbon monoxide (CO) from the 115 GHz centre for Astrophysics survey of CO[50]. The emission maps are decomposed into Galactocentric annuli via the relation,

  $$V_{\rm LSR} = \left(V(R)\frac{R_\odot}{R} - V(R_\odot) \right) \sin(l)\cos(b), \tag{4}$$

  where $V_{\rm LSR}$ is the radial velocity, relative to the local standard of rest, of the gas at Galactocentric radius R with orbital velocity $V(R)$ observed in the direction (l, b) and $R_\odot$ is the distance of the Sun to the Galactic centre. We assumed a spin temperature of $T_S = 170\,\mathrm{K}$ throughout the Galaxy and $R_\odot = 8.25$ kpc. As in ref. 47, for CO, we assigned all high-velocity emission in the innermost annulus. For HI and the other CO annuli, the annuli decomposition interpolation method does not produce a reliable map of the gas column density as kinematic resolution is lost near $l = 0^\circ$. In the interpolation approach, the gas column density in the region $|l| < 10^\circ$ was estimated by interpolating within each annulus from the boundaries. Values at the boundaries of the interpolated region were chosen as the mean gas column density within a range of $\Delta l = 5^\circ$ on both sides of the boundary. Each pixel in the interpolated region was then renormalised to preserve the total gas column density in each line of sight.

- Hydrodynamic approach: this method was pioneered by ref. 10. See also ref. 51 for discussion regarding the construction of the HI map. The presence of non-circular motion in the inner Galaxy provides kinematic resolution towards the GC. Outside the solar circle, pure circular motion with velocities described by equation (4), was assumed with an additional correction for the motion of the Sun relative to the local standard of rest. This meant there was lack of CO and HI gas placed in the outer annuli. We corrected for this by interpolating the outer annuli pixels in the line-of-sight maps which have $|l| < 15^\circ$ and then normalised each pixel to preserve the total gas column density in each line of sight. For CO we interpolated beyond 10 kpc and for HI we interpolated beyond 8 kpc from the GC.

The results of the two methods are compared in Supplementary Fig. 2. Note that in the interpolated approach, if the gas is placed above a certain height above the Galactic plane, it is assumed to be local[47]. This height differs between the gas distributions and was chosen to be 1 kpc for HI and 0.2 kpc for CO. This explains the high latitude CO gas difference in the 3.5–8.0 kpc and 8–10 kpc range of Supplementary Fig. 2. Somewhat broader radii were used in comparison to ref. 47 and 8 as we were fitting to a much smaller region of interest (ROI) and so the data we used had less constraining power and so broader annuli were needed.

Dust Correction Templates: Molecular hydrogen that is not well mixed with carbon monoxide will not be traced by the CO 2.6 mm emission. Furthermore, assuming a constant atomic hydrogen spin temperature $T_S = 170\,\mathrm{K}$ can give an incorrect estimate of column density as the spin temperature can vary along a line of sight. To correct for these deficiencies we included dust templates based on the methods used in ref. 47. Infrared thermal emission from dust provides an alternative method of tracing hydrogen gas in the Milky Way. The correction templates are obtained by subtracting the components of the dust emission that are correlated with the gas already traced by 21 cm and 2.6 mm emission.

We applied this method to $E(B-V)$ reddening maps[52]. Regions that are densely populated by infrared point sources (or potentially a collection of unresolved point sources) could contaminate the $E(B-V)$ reddening map, resulting in an over estimation of the dust column density. To mitigate this, we apply a magnitude cut of 5 mag and higher to the $E(B-V)$ reddening maps. After subtracting the components of the $E(B-V)$ map that were linearly correlated with the hydrogen gas maps, the residuals were separated into positive and negative components. The positive residuals physically represent hydrogen that is not traced by the relevant emission, known as the dark neutral medium, or an over estimation of the atomic hydrogen spin temperature. Negative residuals represent an underestimation of the spin temperature. The results are displayed in Supplementary Fig. 3.

Inverse Compton Emission Template: Whereas the bremsstrahlung and π^0-decay components can be adequately described by the gas maps described above, there is no analogous empirical template for the Galactic IC emission. We use the GALPROP package v54.1[30] to generate such a template. The authors of ref. 47 did a comprehensive comparison of 128 different GALPROP models with all sky Fermi-LAT data. They found a range of possible values for the input GALPROP parameters that are consistent with gamma-ray and local measurements of cosmic-ray data. In this work, we consider the IC template generated with GALDEF file `galdef_54_Lorimer_z10kpc_R20kpc_Ts150K_EBV2mag` as our reference model[47]. As seen from Supplementary Fig. 8, the IC component is of much smaller intensity compared to the interstellar gas diffuse Galactic emission components.

Loop I Template: Loop I is a bright, large angular scale, non-thermal structure. Obtaining a precise template of this source is not possible since its gamma-ray emission is not well traced by radio emission. Following the same approach taken in recent studies by the Fermi Collaboration[24], in this work we used a geometrical template proposed by ref. 53 which is based on a polarization survey at 1.4 GHz (see Supplementary Fig. 4). We adopted the same morphological parameters for the shells assumed in ref. 24.

Sun and Moon emission Templates: In order to account for the diffuse emission from these objects, we construct specialized templates for our ROI by making use of the `gtsuntemp`[54] tool. We used as input the intensity profiles `lunar_profile_v2r0.fits` and `solar_profile_v2r0.fits` available at the *Fermi Science Support Center* website. The templates were constructed in Galactic coordinates with a Cartesian projection method. We note that the templates obtained with the use of this tool depend on the data selection. As such, we did not use the Sun and Moon templates that come with the 3FGL[11] as those were constructed for analysis of only 4 years of data.

2. Mixture Distributions

Wilks' theorem states that the asymptotic distribution of TS is given by Chi squared distribution (χ^2_q) where q is the number of new parameters. This can be used to evaluate a p-value $[1 - p(\mathrm{TS} > \mathrm{TS}_{\mathrm{thresh}})]$ of some threshold value of TS above which the new parameters are accepted as being statistical significant. However, this theorem does not hold if any of the null values of the new parameters are on the boundary of the allowed parameter space. This is problematic for when one wants to decide whether there is a new source in the data which can only have a non-negative amplitude. This limitation can be alleviated using the Chernoff theorem[55] which implies that if the new parameter is the proposed source's amplitude then the TS distribution will be given by a mixture distribution:

$$p(\mathrm{TS}) = \frac{1}{2}(\delta(\mathrm{TS}) + \chi^2_1(\mathrm{TS})). \tag{5}$$

where δ is the Dirac delta function. This formula just states that under the null hypothesis, half the time the evaluated amplitude will be negative (in which case TS is assigned) and the other half of the time (when the amplitude is non-negative) the distribution will follow from Wilks' theorem. This method was shown to work well for simulations of EGRET data by ref. 33. They also proposed that an extension which includes parameters for the two dimensional position of the source has a distribution of

$$p(\mathrm{TS}) = \frac{1}{2}(\delta(\mathrm{TS}) + \chi^2_3(\mathrm{TS})) \tag{6}$$

which they checked is correct by comparing to simulated EGRET data. In some cases sources are found to significantly prefer a curved spectrum[11]. For example, pulsars generally have an exponential cut-off spectrum. Therefore, it may be preferable to test for some new source with a non-parametric spectrum so as not too cause any bias by using a spectrum different from the spectrum the source has. This can be done by doing a bin by bin analysis where the energy range is broken up into a number of bins. If the bins are made sufficiently small, then a power law with Γ set to some fixed value (such as 2) can be used in each bin without loss of generality. Although, the bins shouldn't be too small otherwise one starts to get correlations between the different energy bins due to the finite energy dispersion of the Fermi-LAT instrument[56]. For the case of a testing for a new source at a fixed position we can use $\mathrm{TS} = \sum_{i=1}^{n} \mathrm{TS}_i$ where TS_i is the TS for bin i and there are n bins. We can then utilize the formula given in case 9 of ref. 46:

$$p(\mathrm{TS}) = 2^{-n}\left(\delta(\mathrm{TS}) + \sum_{i=1}^{n}\binom{n}{i}\chi^2_i(\mathrm{TS})\right) \tag{7}$$

where the amplitude in each energy bin needs to be non-negative. This equation has a simple interpretation in terms of mixture distributions. The 2^{-n} term is equal to the number of distinct ways n bins could have a non-negative or negative best fit amplitude. As there is only one way they could all have a negative amplitude, that is the weight of the δ function. While if the there are i non-negative amplitudes they would have $\binom{N}{i}$ distinct configurations and each of these configurations would have a χ^2_i distribution. As discussed in the Methods section, we used equation (7) in testing for new extended sources.

When testing for new point sources, the two position variables of the proposed new point source should also be included. They are not on the boundary of the allowed range under the null hypothesis. Case 9 of ref. 46 also covers the case where n of the new variable are restricted and two are not:

$$p(\mathrm{TS}) = 2^{-n}\left(\sum_{i=0}^{n}\binom{n}{i}\chi^2_{i+2}(\mathrm{TS})\right). \tag{8}$$

However, this formula is not quite the one we are looking for as when all the bins have non-positive best fit amplitudes, we need to have $\mathrm{TS} = 0$ regardless of the values of the position variables. Therefore, in order to modify equation (8) for our case of interest, we need to subtract off $2^{-n}\binom{N}{0}\chi^2_2 = 2^{-n}\chi^2_2$ and add on a $2^{-n}\delta(\mathrm{TS})$ term. This gives equation (2) of the Methods section.

3. Fermi Bubbles

In ref. 24, the spectrum of the Fermi bubbles was determined from the residuals in the energy range between 0.7 GeV and 10 GeV. They examined an area near the southern edge of the Fermi bubbles ($-55^\circ < b < -40^\circ$ and $-15^\circ < l < 15^\circ$). A power-law fit in this region had a spectral index index 1.9 ± 0.1. In contrast, we found our X-bulge and nuclear bulge, for the same energy range, had a power-law fit with a softer spectral index of 2.20 ± 0.05. Also, we estimate the X-bulge plus nuclear bulge has a solid angle of 0.03 sr, and therefore a luminosity per solid angle of $(1.0 \pm 0.1) \times 10^{38}$ erg/s/sr. By contrast, the Fermi bubbles, for $|b| \geq 10^\circ$, have a solid angle of about 0.7 sr and a luminosity[24] per solid angle of $(6.3 \pm 0.1) \times 10^{37}$ erg/s/sr. Even taking a wide range of systematic effects into account, the highest luminosity[24] per solid angle for the Fermi bubbles was only 8.6×10^{37} erg/s/sr.

Ref. 3 used a spectral decomposition technique to determine the low latitude Fermi bubble contribution. However, their residuals for their GCE show the characteristic X-shape in their Fig. 3. Also, they found the addition of their Fermi bubbles template did not remove the need for an extra template to explain the GCE. In summary, current spatial and spectral evidence seems to disfavour a Fermi-bubbles explanation for all of the X-bulge and nuclear bulge emission.

Supplementary References

49. Kalberla, P. M. W. *et al.* The Leiden/Argentine/Bonn (LAB) Survey of Galactic HI. Final data release of the combined LDS and IAR surveys with improved stray-radiation corrections. *Astron. Astrophys.* **440**, 775–782 (2005). astro-ph/0504140.
50. Dame, T. M., Hartmann, D. & Thaddeus, P. The Milky Way in Molecular Clouds: A New Complete CO Survey. *Astrophys. J.* **547**, 792–813 (2001). astro-ph/0009217.
51. Delahaye, T., Fiasson, A., Pohl, M. & Salati, P. The GeV-TeV Galactic gamma-ray diffuse emission I. Uncertainties in the predictions of the hadronic component. *Astron. Astrophys.* **531**, A37 (2011). 1102.0744.
52. Schlegel, D. J., Finkbeiner, D. P. & Davis, M. Maps of Dust Infrared Emission for Use in Estimation of Reddening and Cosmic Microwave Background Radiation Foregrounds. *Astrophys. J.* **500**, 525–553 (1998). astro-ph/9710327.
53. Wolleben, M. A New Model for the Loop I (North Polar Spur) Region. *Astrophys. J.* **664**, 349–356 (2007). 0704.0276.
54. Johannesson, G., Orlando, E. & for the Fermi-LAT collaboration. Accounting for the Sun and the Moon in Fermi-LAT Analysis. *ArXiv e-prints (arXiv:1307.0197)* (2013). 1307.0197.
55. Chernoff, H. On the Distribution of the Likelihood Ratio. *The Annals of Mathematical Statistics* **25**, 573–578 (1954). URL http://links.jstor.org/sici?sici=0003-4851%28195409%2925%3A3%3C573%3AOTDOTL%3E2.0.CO%3B2-P.
56. Ackermann, M. *et al.* The Fermi Large Area Telescope On Orbit: Event Classification, Instrument Response Functions, and Calibration. *Astrophys. J. Supp.* **203**, 4 (2012). 1206.1896.

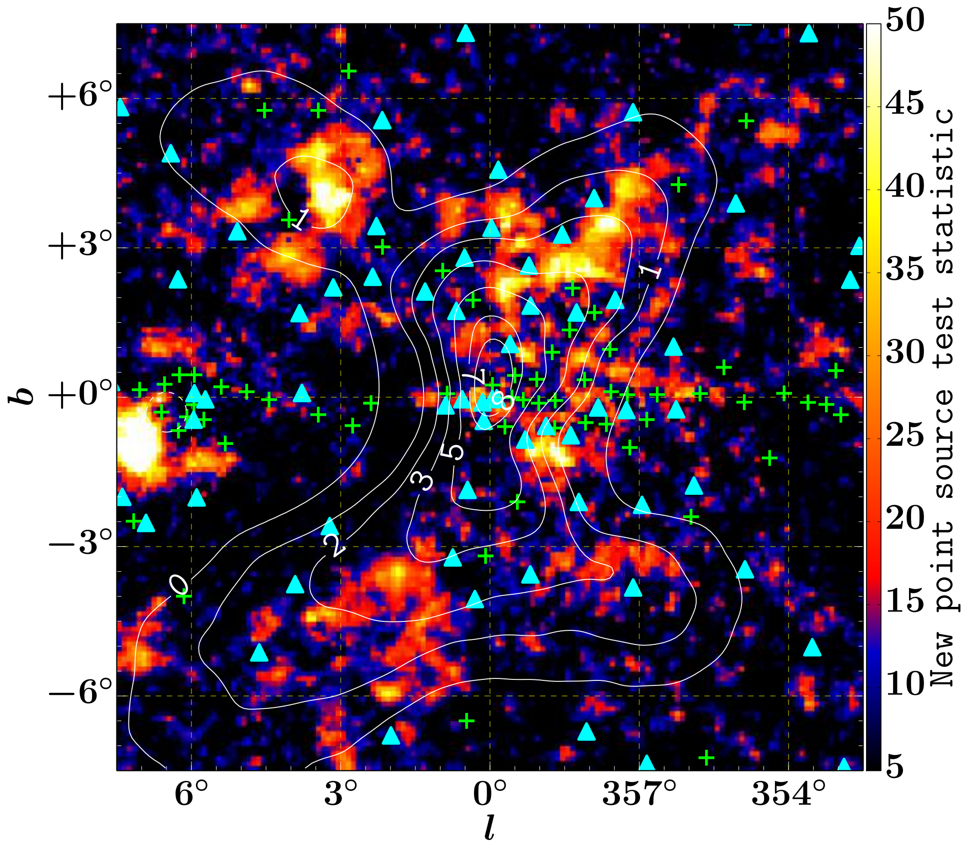

Supplementary Figure 1: Significance map of the $15^\circ \times 15^\circ$ region about the GC output from the gttsmap tool after the new point sources have been identified. The energy range shown is 667 MeV−158 GeV. The 3FGL point sources (cyan triangles) and the new point sources (green crosses) are displayed. Supplementary Table 1 summarizes the basic properties of the new point sources. The white contours are the best-fit model counts from the X-bulge map obtained from analyses of WISE[19] infrared data after convolution the Fermi-LAT instrument response function.

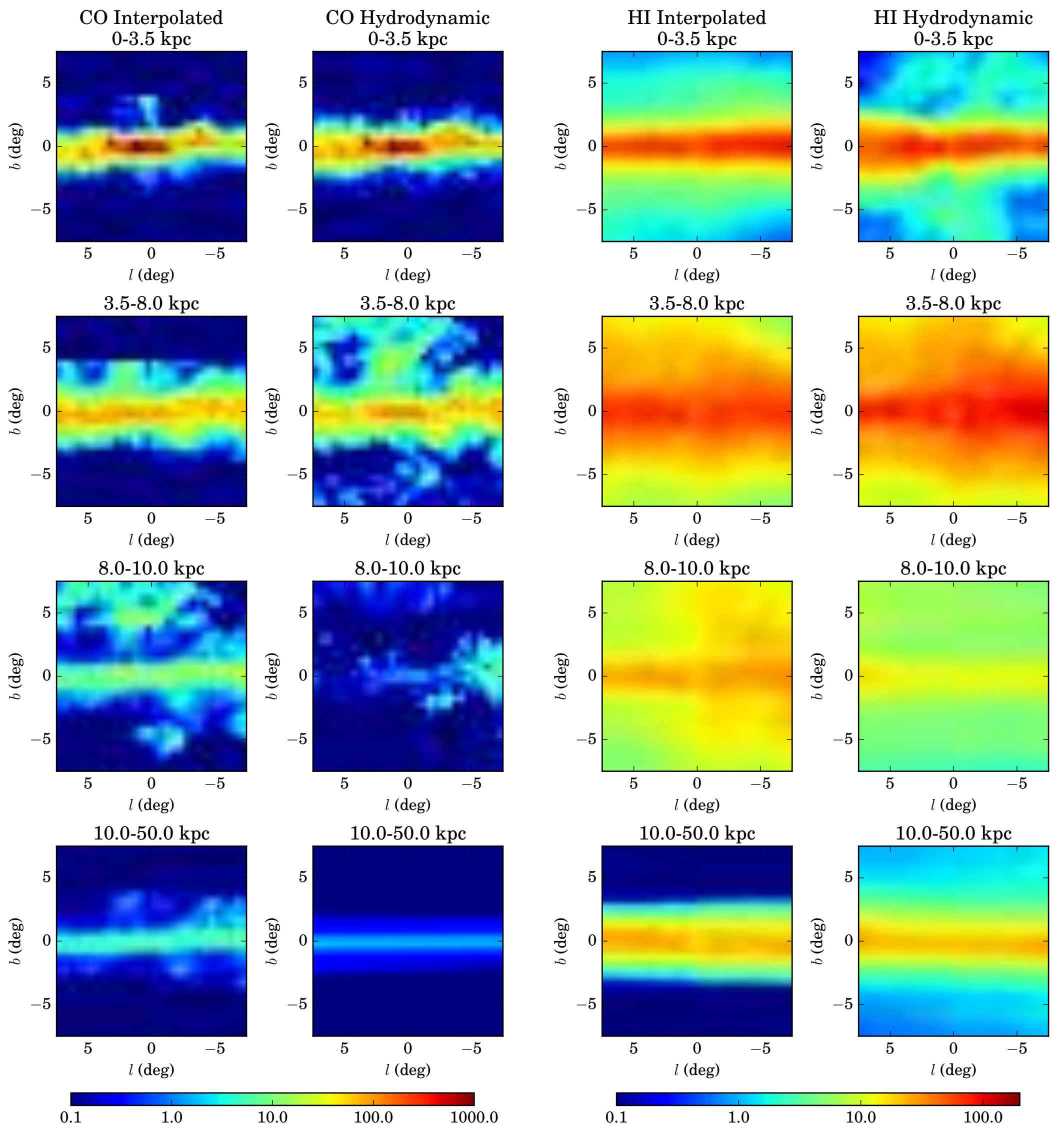

Supplementary Figure 2: Column density maps for the interpolated and hydrodynamic methods. The minimum and maximum radii of each annulus is listed. The units for the H_2 proportional CO maps are K·km/s. The units for the HI maps are $10^{20}\mathrm{cm}^{-2}$.

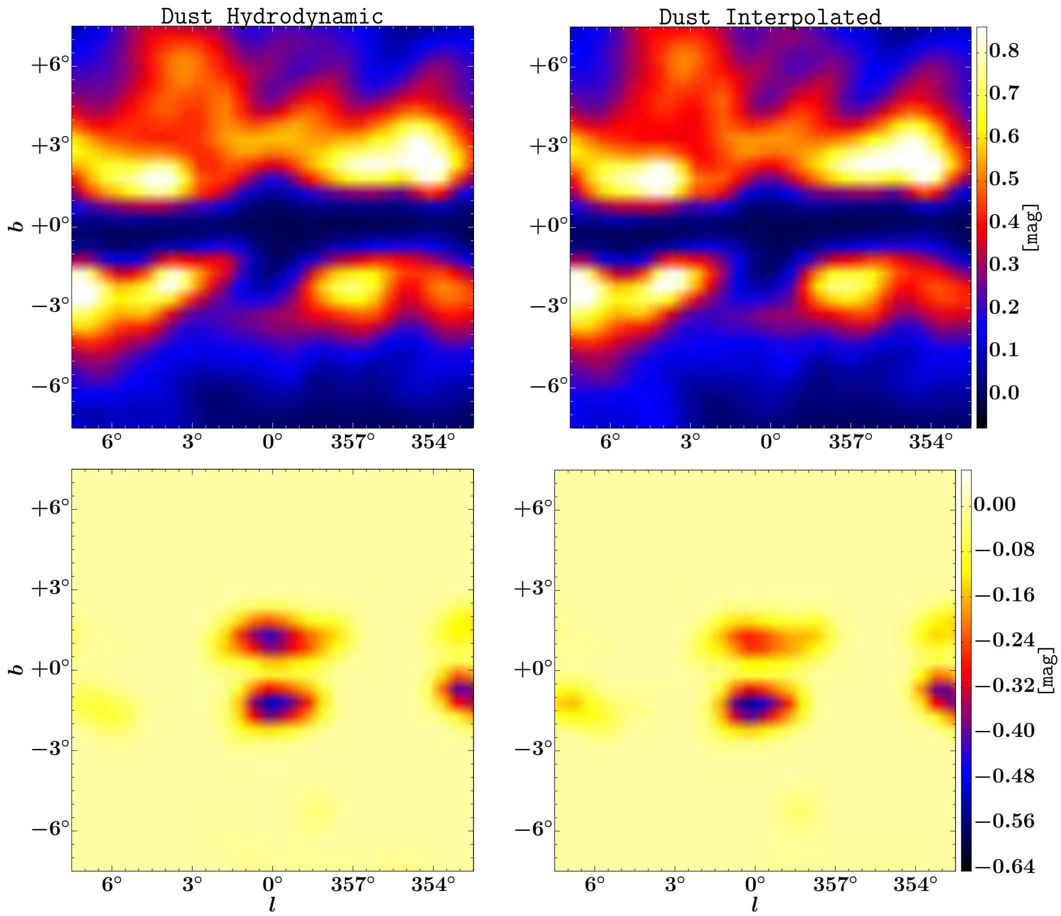

Supplementary Figure 3: Dust reddening E(B-V) positive (top) and negative (bottom) residual maps. The left (right) hand side maps were based on fitting the hydrodynamic (interpolated) HI and CO maps to the E(B-V) reddening map which had be a magnitude cut of 5 mag and higher. For display purposes, Gaussian smoothing with a radius of $0.5°$ was performed.

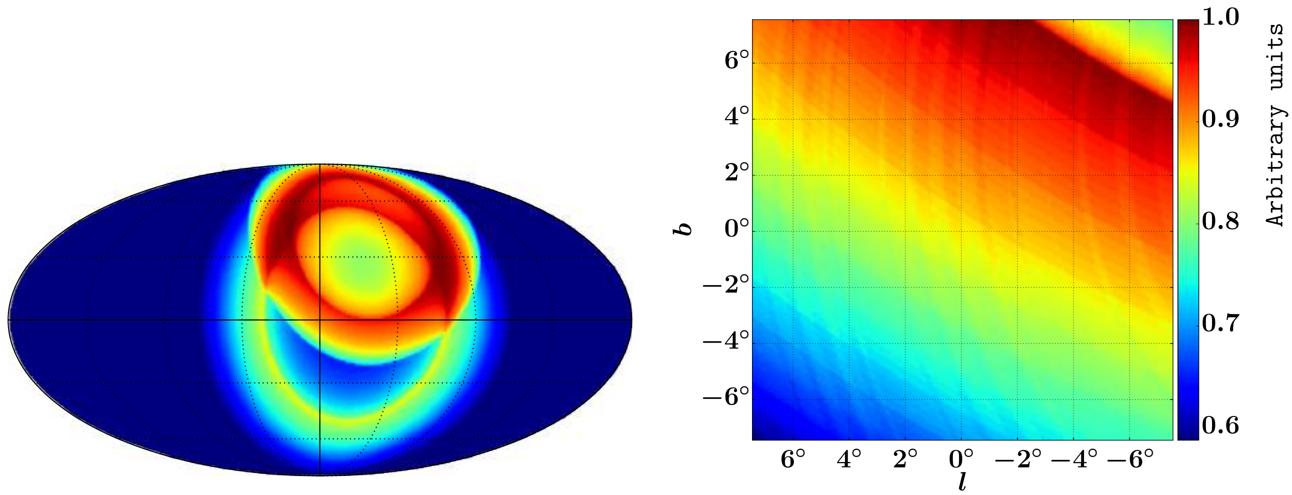

Supplementary Figure 4: Loop I template adapted from ref. 53. A histogram equalized colour mapping is used for display. The map is appropriately normalized, in our region of interest, for analysis with the Fermi Science Tools. On the left we show a full sky version of the map in the Mollweide projection and on the right we have zoomed in to our region of interest.

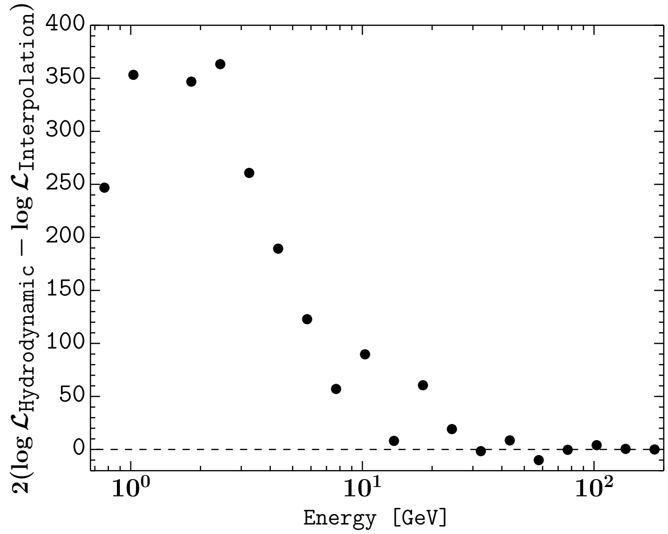

Supplementary Figure 5: Comparison of the log-likelihood obtained for two different interstellar gas models. The likelihood is compared for hydrodynamic[10] gas maps vs the interpolation ones used in the standard Galactic diffuse emission model. Summing over the energy bins gives $\mathrm{TS}_{\mathrm{Hydrodynamic}} = 2 \times 1362$.

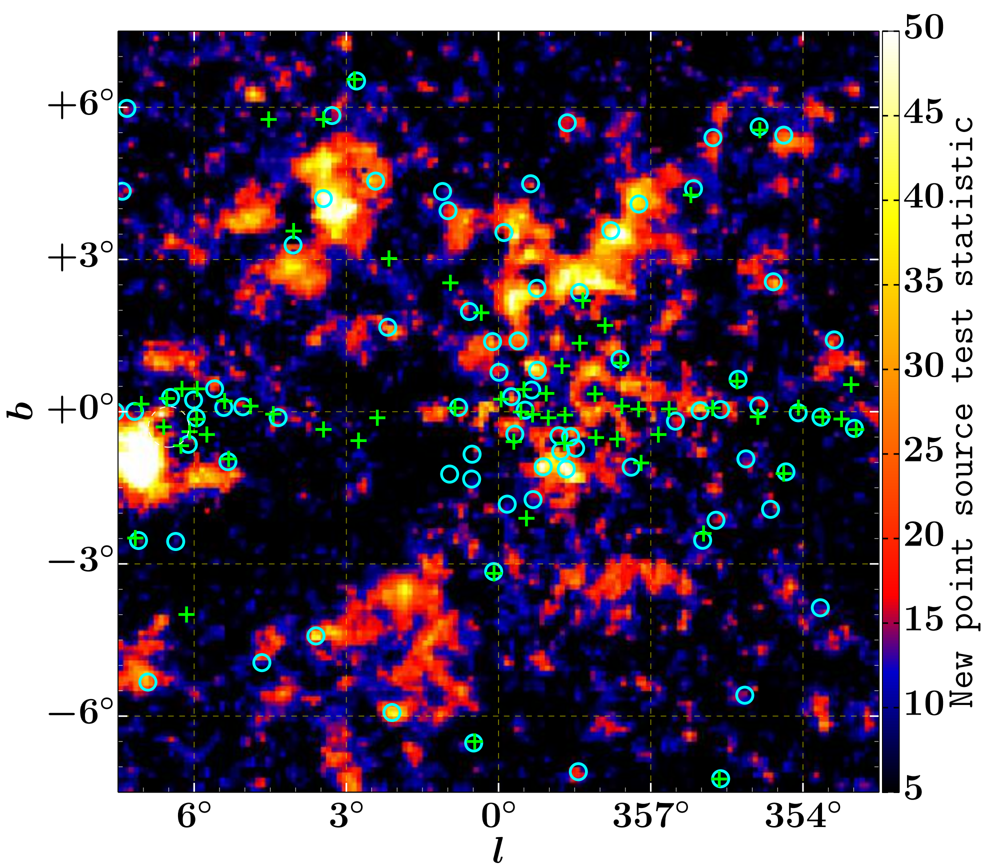

Supplementary Figure 6: Comparison of new gamma-ray point sources in this work vs new point sources in the 2FIG catalog[41]. See caption of Supplementary Fig. 1 for a description of this residual TS map. Cyan circles display the 81 new gamma-ray point sources (not already present in the 3FGL[11]) found in the 2FIG catalog[41]. Green crosses correspond to the 64 new point sources found in this work. Despite the different data sets and background models used in both studies, our analysis confirms the existence of 31 of the new point sources found in 2FIG (see Supplementary Table 1). Note that many undetected 2FIG point source candidates are placed in hot spots in this residual map. It is very likely that by augmenting the time and the photon energy range utilized in this analysis to the same levels used in the 2FIG analysis, such hot spots would be found with greater TS-values and would therefore constitute positive point source detections.

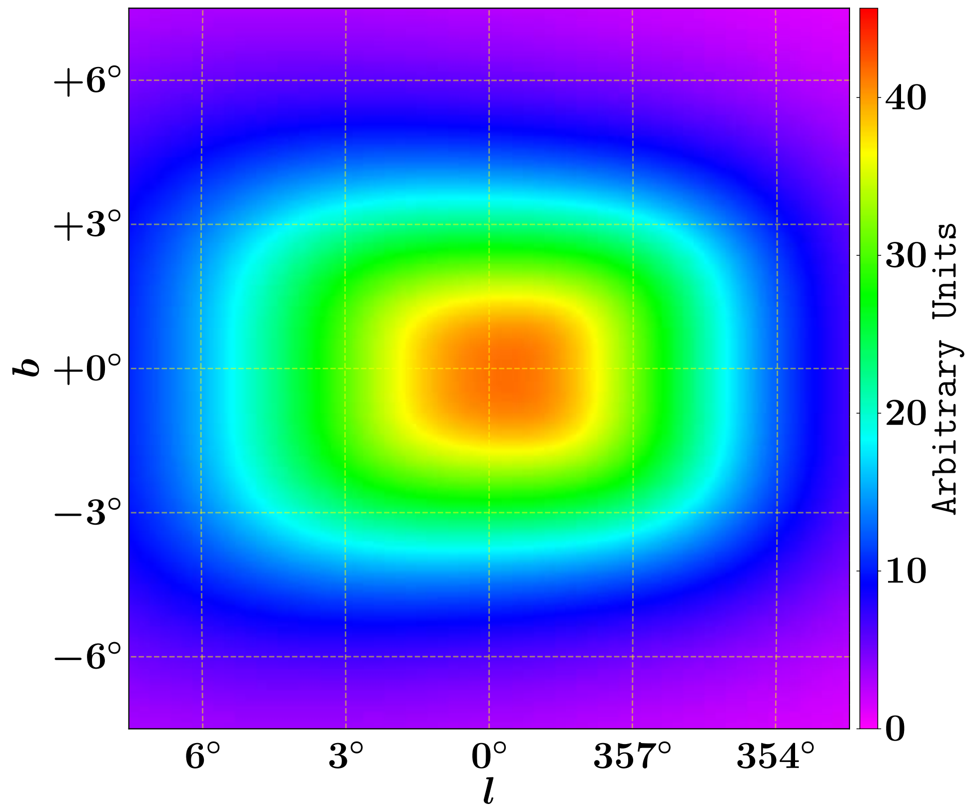

Supplementary Figure 7: The Boxy bulge template obtained from a parametric fit to diffuse infrared DIRBE data[42].

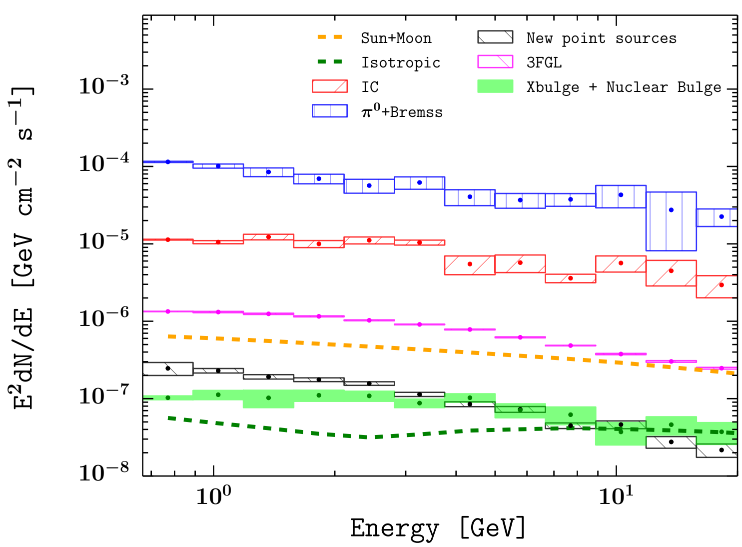

Supplementary Figure 8: Model components. Differential flux of the different components in the $15^\circ \times 15^\circ$ region about the Galactic Center. The normalisations are for the full sky. The model considered in the fit is the *baseline+NP+nuclear bulge+X-bulge* model. To reduce clutter the spectrum of the combined $\mathrm{H_I}$, CO, and dust maps maps are shown as π^0+Bremss. The Loop I spectrum had a low signal to noise for the majority of the bins and so has not been included in the above plot. The box heights represent the 68% confidence interval regions.

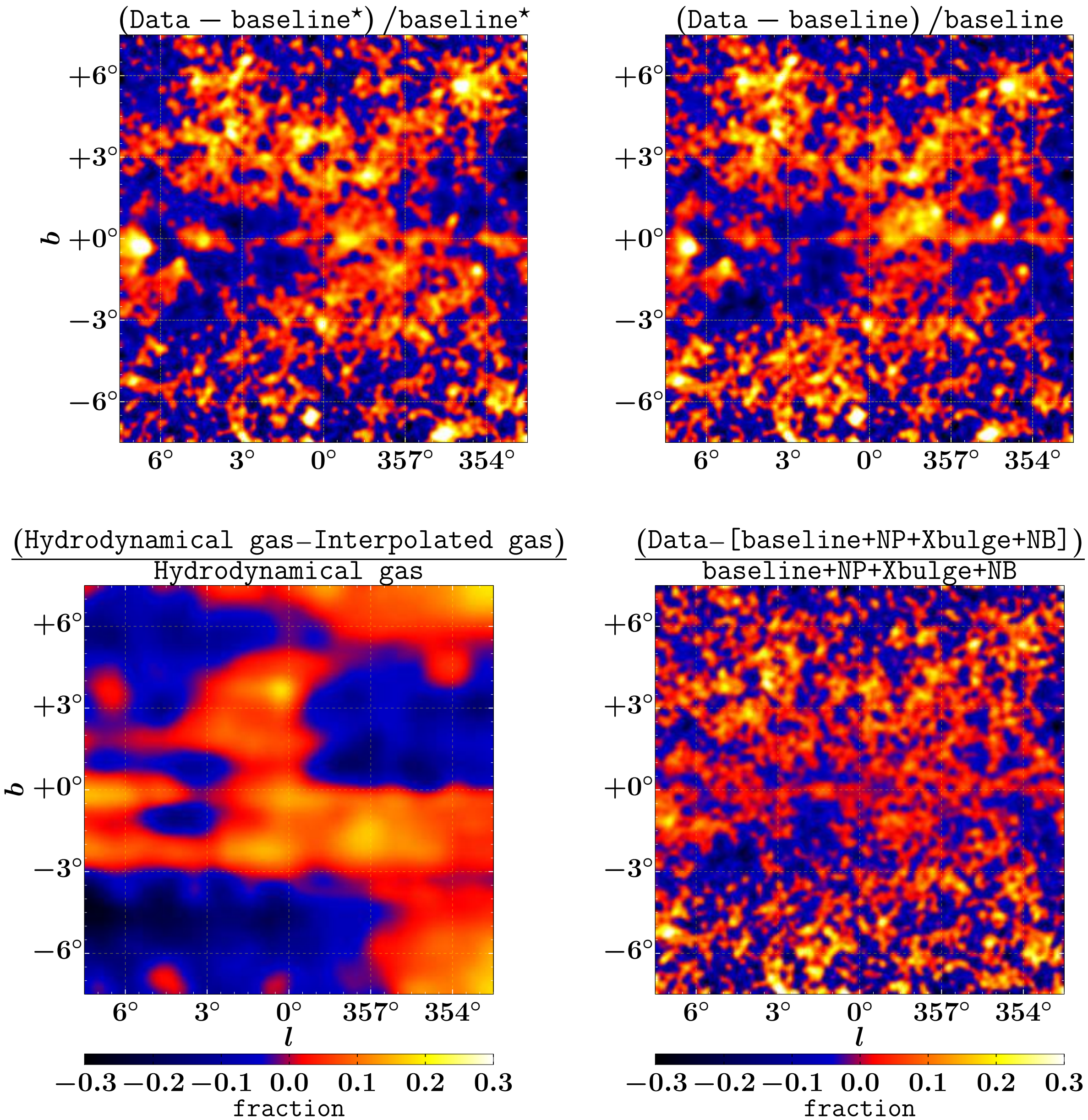

Supplementary Figure 9: Fractional residuals for $E \geq 667$ MeV: Top left: The *baseline** model consists of all 3FGL point sources in the ROI, Loop I, an IC template predicted by GALPROP, the interpolation based gas maps, the recommended isotropic emission map, and a model for the Sun and the Moon. Top right: The *baseline* model is same as the top left, except that it uses the hydrodynamical based gas maps. Bottom left: the fractional difference between the best fit interpolation based and the hydrodynamical gas maps. Bottom right: Our full model (*baseline*+*NP*+*Xbulge*+*NB*) consisting of the baseline plus the 64 new point sources (NP), an infrared X-bulge template tracing old stars in the Galactic bulge, and a Nuclear Bulge (NB) template. For display purposes, we smoothed these images with a 0.1° Gaussian filter.

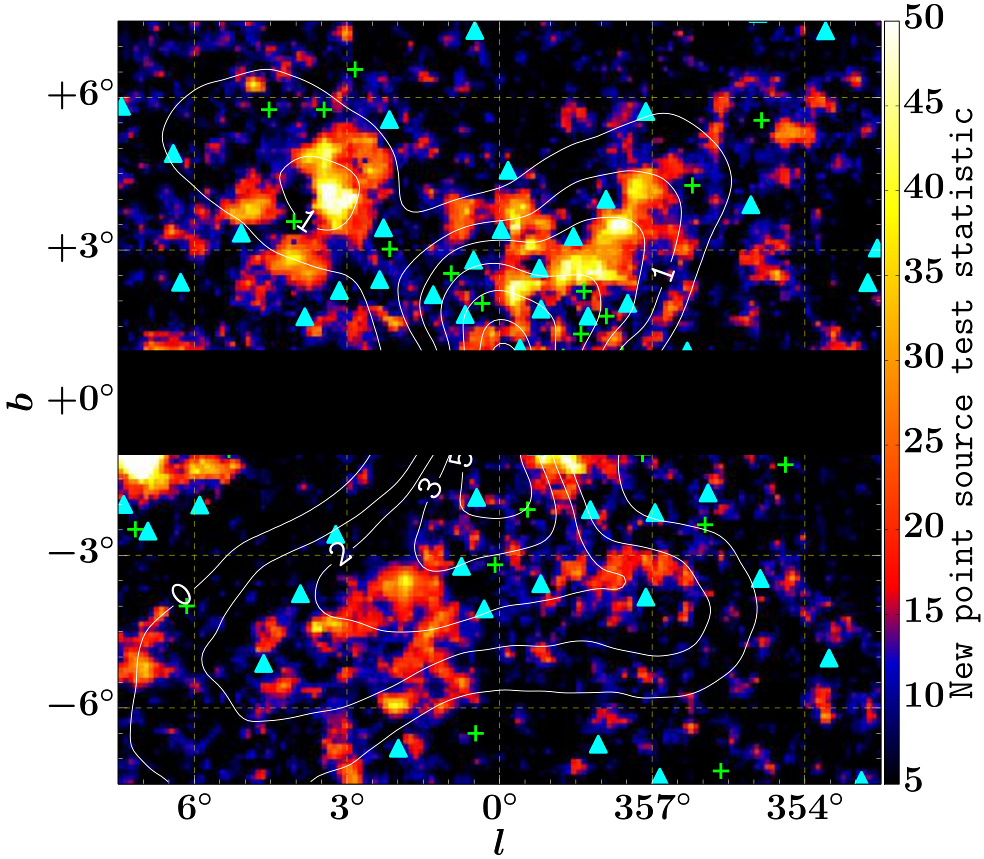

Supplementary Figure 10: Masking of the Galactic plane ($|b| < 1°$)**.** This image displays the ROI for one of our systematic error analyses. The unmasked region contains 22 new point sources. More details of this pipeline are given in the Methods Section and Supplementary Table 4.

Supplementary Table 1: Point Sources detected with $TS \geq 41.8$ for the $15^\circ \times 15^\circ$ region about the Galactic Center.

Name	l [deg]	b [deg]	Association or spatial overlap	TS	$F_{1-100\,\mathrm{GeV}}$ $\times 10^{-9}$ [ph cm^{-2} s^{-1}]	Spectrum
FGC 1711.3 -3008	354.9	5.6	2FIG J1711.0-3005	78.2	2.5 ± 0.3	1.9 ± 0.2
FGC 1719.7 -2947	356.2	4.3	2FIG J1719.1-2945	47.7	1.9 ± 0.3	2.2 ± 0.4
FGC 1725.9 -3429	353.1	0.5		55.7	5.7 ± 0.8	2.6 ± 0.2
FGC 1727.7 -2302	2.8	6.6	2FIG J1727.7-2305	71.5	1.3 ± 0.2	1.9 ± 0.1
FGC 1729.1 -3443	353.2	-0.1	1FIGJ1728.6-3433	109.2	5.4 ± 3.4	2.7 ± 0.3
FGC 1729.2 -3504	353.0	-0.4	2FIG J1729.1-3501, 1FIGJ1729.1-3502	52.7	2.6 ± 16.9	1.9 ± 0.4
FGC 1729.9 -3423	353.6	-0.1	2FIG J1730.0-3421	57.2	4.9 ± 0.9	2.7 ± 2.8
FGC 1730.5 -3353	354.1	0.1	2FIG J1730.8-3356, 1FIGJ1730.2-3351, G354.1+0.1 [39], PSR J1730-3350 [37]	113.2	9.8 ± 0.8	3.2 ± 0.2
FGC 1731.6 -3235	355.3	0.6	2FIG J1731.3-3235, 1FIGJ1731.3-3235, G355.4+0.7 [39]	143.3	15.1 ± 0.8	0.0 ± 0.0
FGC 1732.1 -2257	3.5	5.8	2FIG J1731.3-2303	49.6	1.7 ± 0.3	2.3 ± 0.7
FGC 1733.1 -2910	358.3	2.2	2FIG J1732.6-2901	71.3	3.4 ± 0.5	2.2 ± 0.4
FGC 1733.3 -3318	354.9	-0.1	Liller 1 [38]	57.4	4.6 ± 0.8	2.8 ± 0.2
FGC 1733.9 -2948	357.9	1.7		55.8	1.3 ± 0.4	2.3 ± 0.2
FGC 1734.6 -2202	4.5	5.8		73.7	2.1 ± 0.3	1.9 ± 0.5
FGC 1734.9 -3228	355.8	0.1	2FIG J1734.6-3237, 1FIGJ1734.6-3228, G355.60.0 [39]	91.3	8.8 ± 0.8	2.6 ± 0.3
FGC 1735.1 -3028	357.6	1.0	2FIG J1735.7-3025, 1FIGJ1735.4-3030, Terzan 1 [38]	163.3	8.0 ± 0.7	$1.9 \pm 0.2,\ 5.9 \pm 1.3$
FGC 1736.5 -2934	358.4	1.4		44.2	3.3 ± 0.6	2.4 ± 0.2
FGC 1736.5 -3420	354.4	-1.2	2FIG J1736.2-3422, 1FIGJ1736.1-3422	101.9	3.3 ± 0.5	$1.9 \pm 0.1,\ 5.7 \pm 1.1$
FGC 1737.2 -3145	356.6	0.1	1FIGJ1737.4-3144	177.7	12.0 ± 0.9	2.4 ± 0.4
FGC 1738.1 -2647	1.0	2.5	PSR J1801-2451 [37]	43.1	1.7 ± 0.5	2.4 ± 0.6
FGC 1738.7 -3115	357.2	0.1		49.6	3.3 ± 0.9	2.0 ± 1.8
FGC 1738.9 -2737	0.3	2.0		50.4	1.7 ± 0.5	2.1 ± 0.7
FGC 1739.1 -2931	358.8	0.9		84.5	5.1 ± 0.7	1.9 ± 0.4
FGC 1739.2 -2530	2.2	3.0		56.2	2.7 ± 0.5	2.3 ± 0.4
FGC 1739.3 -3056	357.6	0.1	1FIGJ1740.1-3057	111.3	9.5 ± 1.0	2.6 ± 0.4
FGC 1739.6 -3022	358.1	0.4	1FIGJ1739.4-3010, PSR J1739-3023 [37]	363.3	12.5 ± 0.9	1.9 ± 2.3
FGC 1739.7 -3151	356.9	-0.5		48.0	2.9 ± 0.8	2.9 ± 0.5
FGC 1741.1 -2932	359.1	0.4		50.0	3.0 ± 1.1	2.0 ± 0.9
FGC 1741.5 -2337	4.0	3.6		50.3	2.2 ± 1.7	$1.9 \pm 0.6,\ 1.5 \pm 0.3$
FGC 1742.1 -3050	358.1	-0.5		66.3	5.6 ± 1.0	2.7 ± 0.2
FGC 1742.1 -3112	357.7	-0.5		46.7	3.0 ± 0.8	$1.9 \pm 0.2,\ 1.8 \pm 0.2$
FGC 1742.7 -2907	359.5	0.4	2FIG J1742.3-2916	90.4	4.7 ± 1.2	2.4 ± 0.8

The full version of this table is also provided as a FITS file in the supplementary online material. The third column displays 1FIG[31] and 2FIG[41] associations as well as spatial overlaps with tentative multi-wavelength counterparts. We use the globular cluster catalog[38], ATNF pulsar catalog[37], Green's SNR catalog[39], and the Roma-BZCAT blazar catalog[40]. Best-fit fluxes were obtained in the $1-100$ GeV energy range are denoted by $F_{1-100\,\mathrm{GeV}}$. The spectrum column gives the spectral slope for a power law fit, except in the case where an exponential cutoff model was preferred at $\geq 4\sigma$ level where the E_{cut} in GeV units is also given. Similarly to ref. 11, we combined our energy bands into four larger bands before fitting the spectrum. The errors are 1σ.

Supplementary Table 2: Radial distribution of X_{CO} as obtained from our maximum likelihood estimation using the hydrodynamic gas template models.

Annulus	$0-3.5$ kpc	$3.5-8.0$ kpc	$8.0-10.0$ kpc
X_{CO}	0.4 ± 0.1	1.0 ± 0.2	3.9 ± 1.3

The quoted values are for the first three annuli and are in units of $10^{20}[\text{ cm}^{-2} \text{ (K km s}^{-1})^{-1}]$. The errors are 1σ.

Supplementary Table 3: Systematic likelihood analysis results

Base	Source	$\log(\mathcal{L}_{\rm Base})$	$\log(\mathcal{L}_{\rm Base+Source})$	$\rm TS_{Source}$	σ	Number of source parameters
baseline+NB+X-bulge	NFW	-171956.4	-171948.7	15	1.5	19
baseline+NFW	NB+X-bulge	-172167.9	-171948.7	438	18.6	2×19
baseline*	NFW	-173565.0	-172929.2	1272	34.6	19
baseline*+NFW	NB+X-bulge	-172929.2	-172592.0	674	23.8	2×19
baseline*+NB+X-bulge	NFW	-172631.5	-172592.0	79	6.9	19
baseline	2FIG	-172461.4	-170710.5	3501	37.3	81×19
baseline+2FIG	X-bulge	-170710.5	-170487.3	446	19.8	19
baseline+2FIG	NFW	-170710.5	-170484.6	452	19.9	19
baseline+2FIG	NB	-170710.5	-170470.5	480	20.6	19
baseline+2FIG+NB	NFW	-170470.5	-170387.8	165	11.1	19
baseline+2FIG+NB	X-bulge	-170470.5	-170307.6	326	16.6	19
baseline+2FIG+NB+Xbulge	NFW	-170307.6	-170301.8	12	1.1	19

See the caption of Table 1 for definitions. The *baseline** is same as the *baseline* model, except that it uses the interpolated gas maps. 2FIG are the 81 new point sources found in our ROI by ref. 41.

Supplementary Table 4: Likelihood analysis results with a Galactic plane mask

Base	Source	$\log(\mathcal{L}_{\rm Base})$	$\log(\mathcal{L}_{\rm Base+Source})$	$\rm TS_{Source}$	σ	Number of source parameters
baseline	NFW	-430289.1	-430155.5	134	9.8	19
baseline	X-bulge	-430289.1	-430089.2	200	12.5	19
baseline	NP	-430289.1	-429657.8	631	12.9	22×19
baseline+NP	NFW	-429657.8	-429559.9	98	8.0	19
baseline+NP	X-bulge	-429657.8	-429496.6	322	16.5	19
baseline+NP+X-bulge	NFW	-429496.6	-429487.2	19	2	19

See the caption of Table 1 for definitions. After masking the Galactic plane ($|b| < 1^\circ$), the number of new point sources (NP) added to the fit were 22 (see also Supplementary Fig. 10).